and the top and bottom boundaries were stress-free, impermeable, and held at different constant temperatures. There was no internal heating. The thermal and velocity spectra showed at least three to four orders of magnitude decay with wave number along all three directions, indicating adequate spatial resolution.
12. The equation for conservation of mass takes the form of the anelastic approximation in which the time derivative of the density is neglected. Y. Ogura and N. A. Phillips, *J. Atmos. Sci.* **19**, 173 (1962).
13. The dissipation number D is given by $\alpha gh/C_p$, where α is the thermal expansivity, g is the gravitational acceleration, h is the depth of the mantle, and C_p is the specific heat [see also (*1*)]. The value of Ra_s is given by $\alpha_0 g\Delta Th^3/\nu_0\kappa_0$, where the subscript "0" indicates surface value and κ and ν are, respectively, the thermal diffusivity and the kinematic viscosity.
14. F. H. Busse and H. Frick, *J. Fluid Mech.* **150**, 451 (1985); D. B. White, *ibid.* **191**, 247 (1988); A. C. Fowler, *Stud. Appl. Math.* **72**, 189 (1985); E. Giannandrea and U. R. Christensen, *Phys. Earth Planet. Inter.* **78**, 139 (1993).
15. The temperature-dependent viscosity introduces variable coefficients into the momentum equation, and therefore the momentum equation is solved iteratively with the generalized minimum residual method [Y. Saad and M. H. Schultz, *Soc. Ind. Appl. Math. J. Sci. Stat. Comput.* **7**, 856 (1986)]. Here the depth-dependent part of the momentum equation is treated as a preconditioner to accelerate convergence.
16. The background adiabatic density, ρ_a, varies with nondimensional depth, z, as $[1 + 2(D/\gamma)z]^{1/2}$, where γ is the Grüneisen parameter. Thermal expansivity decreases with density according to $1/\rho_a^6$, as determined experimentally [A. Chopelas and R. Boehler, *Geophys. Res. Lett.* **19**, 1983 (1992)]. Thermal conductivity is modeled as ρ_a^4, following phonon conduction [D. L. Anderson, *Phys. Earth Planet. Inter.* **45**, 307 (1987)].
17. K. Chin-Purcell, Preprint 92-141 (Army High Performance Computing Research Center, Minneapolis, 1992). BOB (Brick of Bytes) is an interactive computer program for volume rendering of 3D data on Silicon Graphics workstations.
18. There are no phase transitions in this model [S. Honda, D. A. Yuen, S. Balachandar, D. Reuteler, *Science* **259**, 1308 (1993)].
19. Disconnected hot plumes are observed in high-*Ra*, constant-viscosity convection in the Boussinesq limit for *Ra* in excess of 10^7 [A. V. Malevsky and D. A. Yuen, *Geophys. Res. Lett.* **20**, 383 (1993)]. The occurrence of this phenomenon marks the transition of convection to the hard-turbulent regime [F. Heslot, B. Castaing, A. Libchaber, *Phys. Rev. A* **36**, 5870 (1987)].
20. It has been conjectured that, because of the low viscosity in hot plumes, viscous heating be regarded as a second-order effect in the dynamics of plumes [D. E. Loper and F. Stacey, *Phys. Earth Planet. Inter.* **33**, 304 (1983)].
21. In studies of convection with depth-dependent thermal expansivity it has been shown that the hot plumes grow in vigor on their way up because of the increase in buoyancy [S. Balachandar, D. A. Yuen, D. M. Reuteler, *Geophys. Res. Lett.* **19**, 2247 (1992); U. Hansen, D. A. Yuen, S. E. Kroening, T. B. Larsen, *Phys. Earth Planet. Inter.* **77**, 205 (1993)].
22. This number comes directly from numerical evaluation of Eq. 2, the viscous dissipation contribution to the energy equation.
23. The amount of internal heating in the mantle due to radioactive decay is $\sim 6 \times 10^{-12}$ W/kg for average concentrations in chondritic meteorites, which can be regarded as primitive mantle material. This internal heating also appears in nondimensional form as an inhomogeneous source term in the temperature equation [A. M. Leitch and D. A. Yuen, *Geophys. Res. Lett.* **16**, 1407 (1989)].
24. In Boussinesq convection models with plates, weakened zones are positioned adjacent to the descending slabs [H. Schmeling and W. R. Jacoby, *J. Geophys. (London)* **50**, 89 (1981); M. Gurnis, *Geophys. Res. Lett.* **16**, 179 (1989); A. Lenardic and W. M. Kaula, *J. Geophys. Res.* **99**, 15697 (1994)].
25. For model 2, the effective Rayleigh number based on mean temperature is given by $Ra_{eff} = 5 \times Ra_s$, whereas, for model 1, because of the depth-dependent properties, $Ra_{eff} = 4 \times Ra_s$. Thus, the behavior of model 2 at $Ra_s = 5 \times 10^4$ is the closest to that of model 1.
26. U. R. Christensen and D. A. Yuen, *J. Geophys. Res.* **94**, 814 (1989); A. V. Malevsky and D. A. Yuen, *Geophys. Astrophys. Fluid Dyn.* **65**, 149 (1992).
27. D. P. McKenzie, J. M. Roberts, N. O. Weiss, *J. Fluid Mech.* **62**, 465 (1974); S. A. Weinstein, P. L. Olson, D. A. Yuen, *Geophys. Astrophys. Fluid Dyn.* **47**, 157 (1989).
28. P. E. van Keken, D. A. Yuen, A. P. van den Berg, *Earth Planet. Sci. Lett.* **112**, 179 (1992); *Geophys. Res. Lett.* **20**, 1927 (1993).
29. R. L. Larson, *Geology* **19**, 547 (1991).
30. We thank V. C. Steinbach and Yu. Yu. Podladchikov for inspiring discussions that provided the stimulus for this work. This research was supported by the Geochemistry Program and the Division of Mathematical Sciences of the National Science Foundation (NSF DMS 92-01042) and by the National Aeronautics and Space Administration.

28 September 1994; accepted 12 December 1994

Visual Appearance of Matte Surfaces

Shree K. Nayar* and Michael Oren

All visual sensors, biological and artificial, are finite in resolution by necessity. As a result, the effective reflectance of surfaces in a scene varies with magnification. A reflectance model for matte surfaces is described that incorporates the effect of macroscopic surface undulations on image brightness. The model takes into account complex physical phenomena such as masking, shadowing, and interreflections between points on the surface, and it predicts the appearance of a wide range of natural surfaces. The implications of these results for human vision, machine vision, and computer graphics are demonstrated with both real and rendered images of three-dimensional objects. In particular, objects with extremely rough surfaces produce silhouette images devoid of shading, precluding visual perception of the object's shape.

Painters and sculptors use their knowledge of the interaction between light and materials (*1*, *2*) to convey compelling shape cues to an observer (*3*). Reflection of light by materials may be viewed as the first fundamental process in visual perception by human or machine. All reflectance mechanisms can be broadly classified into two categories: surface and body. In surface reflection, light rays are reflected at the interface between the surface medium and air. With very smooth surfaces, this results in a specular or mirrorlike appearance, where the viewed surface produces a clear virtual image of its surroundings that is geometrically distorted if the surface is not planar (*4*). The rougher the surface, the more the virtual image becomes blurred, altering surface appearance from shiny to glossy, and even becoming diffuse for very rough surfaces. Surface reflection is common, for instance, in metals.

In body reflection, incident light rays penetrate the surface and are scattered around because of reflections and refractions caused by inhomogeneities within the surface medium. Some of this light energy may be absorbed by the surface or transmitted through it. The remaining light energy finds its way back to the interface to re-emerge as body reflection. As a result of the random subsurface scattering of light, the emerging light rays are distributed in a wide range of directions, giving the surface a matte appearance. Body reflection predominates in materials like clay, plaster, concrete, and paper. In many other materials, however, both surface and body reflection mechanisms coexist and together determine the final visual appearance. Mathematical models for both reflection mechanisms, based on physical and geometrical optics, have been studied extensively.

For body reflection, numerous models have been suggested for the scattering process (*5–7*). Among these, Lambert's law (*5*), proposed in 1760, remains the most widely used in visual psychophysics (*8*), computational vision (*9*), remote sensing (*10*), and computer graphics (*11*). It predicts that the brightness, or radiance, L_r, of an ideal matte surface point is $\frac{\rho}{\pi}\cos\theta_i$, where ρ, the albedo or reflectivity, represents the fraction of the total incident light reflected by the surface, and θ_i is the incidence angle between the surface normal and the illumination direction. The popularity of Lambert's model can be attributed to its ability to predict with a fair degree of accuracy the appearance of a large spectrum of real materials. Another reason is undoubtedly its simple mathematical form, which lends itself to the prediction of numerous interesting appearance properties; for theoreticians and practitioners alike, the use of Lambert's law is a temptation difficult to resist. Both reasons have led to its widespread use in understanding and emulating perception of im-

Department of Computer Science, Columbia University, New York, NY 10027, USA.

*To whom correspondence should be addressed.

portant visual cues such as shading.

The most appealing aspect of Lambert's law is its prediction that the brightness of a scene point is independent of the observer's viewpoint. This in turn can be exploited to establish that a scene point illuminated by several light sources can be considered as being illuminated by a single source of intensity and direction given simply by the centroid of all the sources. Furthermore, the surface normal and albedo of a scene point can be uniquely determined from its brightness values measured with three known illuminants (*12*). The simplicity of Lambert's law permits the analysis of even complex high-order phenomena such as interreflections (*13, 14*), the bouncing of light rays between mutually visible points on a concave surface. In the presence of interreflections, a surface continues to behave exactly like a Lambertian one without interreflections but with a different set of normals and albedo values (*15*).

Alas, our visual world limits the scope of Lambert's model. Though it does well in describing subsurface scattering in a large variety of materials, it cannot describe the ubiquitous interplay between surface undulations and image resolution (Fig. 1). Visual processing by humans and machines relies on finite-resolution sensors. Photoreceptors of the retina and pixels in a video camera are both, by necessity, finite-area detectors; light intensity can be recorded only by counting photons collected in buckets of measurable size. This finite resolution, along with the optical point spread (*16*) inherent to any imaging system, ensures that each receptor receives light not from a single point but rather from a surface area, which increases as the square of the distance of the surface from the eye or the camera (Fig. 1B). Often, substantial macroscopic surface roughness (on a scale much greater than the wavelength of the incident light) is projected onto a single detector, which in turn produces an aggregate brightness value. Whereas Lambert's law may hold for the observation of a single planar facet (near sight), a collection of such facets with different orientations (far sight) is guaranteed to violate Lambert's law. The primary reason for this is the variation in area of the foreshortened facets as the observer moves (Fig. 2A). Analysis of this phenomenon can be traced back almost a century. Past work has resulted in empirical models (*17, 18*) designed to fit experimental data as well as theoretical results derived from first principles (*19–21*). Much of this work was motivated by the non-Lambertian reflectance of the moon (*22–24*). Unfortunately, these models are severely limited in scope either by the specific surface geometry assumed or by their inability to predict brightness for the entire hemisphere of source and sensor directions.

We have developed a reflectance model that describes the relation between macroscopic surface roughness and sensor resolution. The surface patch imaged by each sensor detector is modeled as a collection of long, symmetric, V-shaped cavities (Fig. 2B); each cavity has two planar Lambertian facets with opposing normals, the facet normals are free to deviate from the mean surface normal, and all facets on the surface have the same albedo ρ. It is assumed that the V-cavities are uniformly distributed in orientation ϕ_a (azimuth angle) on the surface plane, whereas facet tilt θ_a (polar angle) is normally distributed with zero mean and standard deviation σ, the latter serving as a roughness parameter (*25*). This isotropic surface model has been used to study surface reflection from rough surfaces (*26*) and is invoked here to achieve mathematical tractability (*27*). When $\sigma = 0$, all facet normals align with the mean surface normal, producing a planar patch that obeys Lambert's law. However, as σ increases, the V-cavities get deeper on the average, and the deviation from Lambert's model increases.

Our reflection model accounts for not only the foreshortening of individual facets (Fig. 2A), but also masking, shadowing, and interreflections (up to two bounces) between adjacent facets (*28*). The brightness of a surface patch is expressed as the integral of facet brightness over all facet normals. This integral is cumbersome to evaluate and must be broken into components representing facets that are

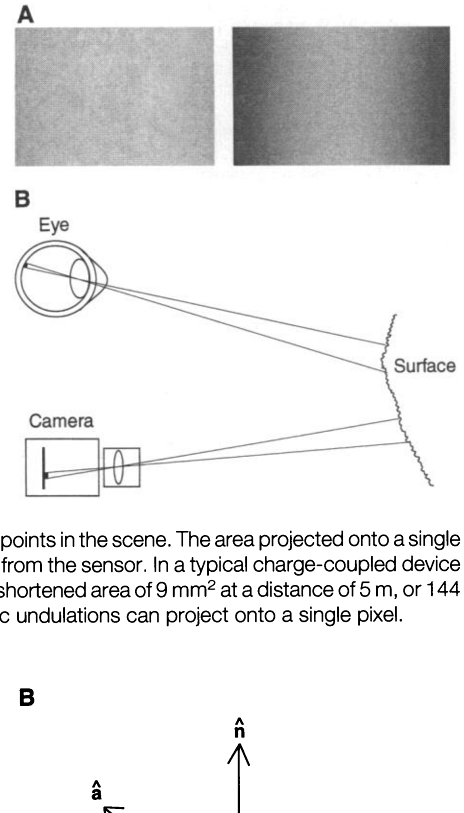

Fig. 1. (**A**) Digital images of two surface patches illuminated from the same direction. The strong shading of the right patch leads the observer to perceive a cylindrical surface with a vertical axis. In contrast, the left patch has fairly uniform brightness, and the lack of shading seems to suggest a planar surface. The actual shapes of the surfaces are identical. Both patches are clipped from images (512 by 480 pixels) of cylindrical vases. The left image is of a real clay vase with a very rough exterior that gives it a flat appearance. The right image is of a vase identical shape, but the image was rendered with Lambert's model (*14*) for body reflection. Lambert's law predicts strong shading and drives brightness at the occluding boundaries to zero. Though it predicts the reflectance of several natural surfaces with adequate accuracy, it fails to account for the interplay between macroscopic surface roughness and sensor resolution. (**B**) Retina of the human eye (*30*) and solid-state sensors in video cameras have finite-size receptors that aggregate brightness from areas rather than points in the scene. The area projected onto a single receptor increases as the square of surface distance from the sensor. In a typical charge-coupled device camera with a 25-mm lens, each pixel image is a foreshortened area of 9 mm^2 at a distance of 5 m, or 144 mm^2 at 20 m. Clearly, large amounts of macroscopic undulations can project onto a single pixel.

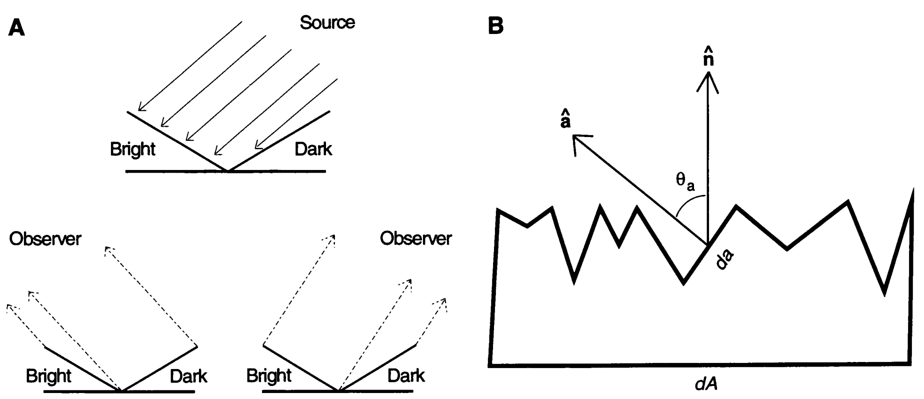

Fig. 2. (**A**) A V-cavity used to illustrate why a collection of Lambertian facets with different orientations does not obey Lambert's law (solid lines, source light; dashed lines, reflected light). When the cavity is illuminated from the right, the smaller incidence angle for the left facet makes it brighter than the right one. For an observer on the left, the foreshortening of the left facet is greater than that of the right one and a larger fraction of the cavity is dark. As the observer moves right, toward the illuminant, the fraction of the brighter area increases, causing the aggregate brightness of the V-cavity to rise. (**B**) A reflectance function is derived by modeling a surface patch as a collection of V-cavities ($da << dA$) with different facet normals ($\hat{\mathbf{a}}$). dA, area of a surface element with many facets; da, facet area; and $\hat{\mathbf{n}}$, vector normal to dA.

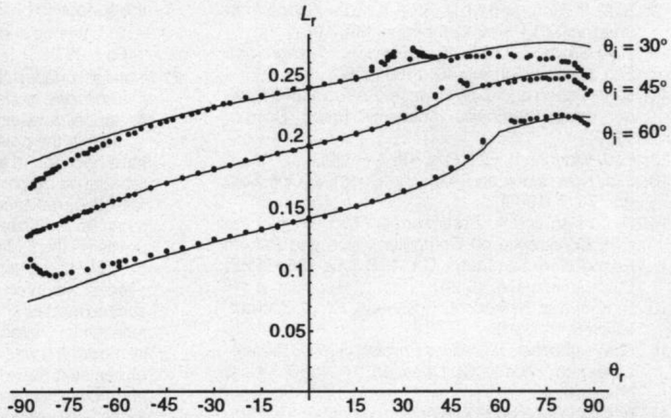

Plaster

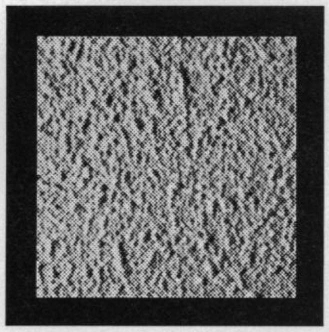

Fig. 3. Measured reflectance (dots) is compared with reflectance predicted by the model (solid lines) for plaster. Surface radiance L_r, computed as an average over the entire surface patch, is plotted as a function of sensor direction θ_r for three angles of incidence θ_i. Albedo ρ and roughness σ were selected to achieve the best fit. In these measurements, the source direction, sensor direction, and the mean surface normal are coplanar ($\phi_i = \phi_r = 0$). Surface brightness increases as the sensor approaches the source direction, violating Lambert's law that predicts brightness to be independent of viewing direction. This brightness increase is also in contrast to surface reflection mechanisms that produce peaks around the specular direction. In these and other experiments (*28*), the proposed model is found to be in strong agreement with measured data. The narrow peak observed in the source direction is attributed to the opposition effect (*30*). This phenomenon is relatively less important to visual perception as it requires the observer and the source to be within a few degrees from each other, a situation difficult to emulate in practice without either one obstructing the view of the other. The scope of the proposed model is broadened by combining it (*28*) with previously suggested ones for surface reflection (*26*) that are based on similar roughness assumptions. Validity of such a combined model was verified with samples such as sand, cloth, foam, sandpaper, and wood.

masked, shadowed, masked and shadowed, and neither masked nor shadowed. The complexity of the integral is easily seen by imagining the different masking and shadowing conditions that arise as a single V-cavity is rotated in the surface plane. We arrived at a solution to the integral by first deriving a basis function for each component of the integral, and then finding coefficients for the bases through extensive numerical simulations (*28*). The accuracy of the model was verified by matching model predictions with reflectance measurements from natural surfaces such as plaster, sand, and clay (Fig. 3). In all cases, predicted and measured data were found to be in strong agreement. A systematic increase in brightness is observed as the sensor moves toward the illuminant; this backscattering is in contrast to Lambertian behavior where brightness is constant and independent of sensor direction, and also in contrast to surface reflection where a peak in brightness is expected in the vicinity of the specular direction (*26*). For applications where simplicity is desired over high precision, approximations were made to arrive at this qualitative model:

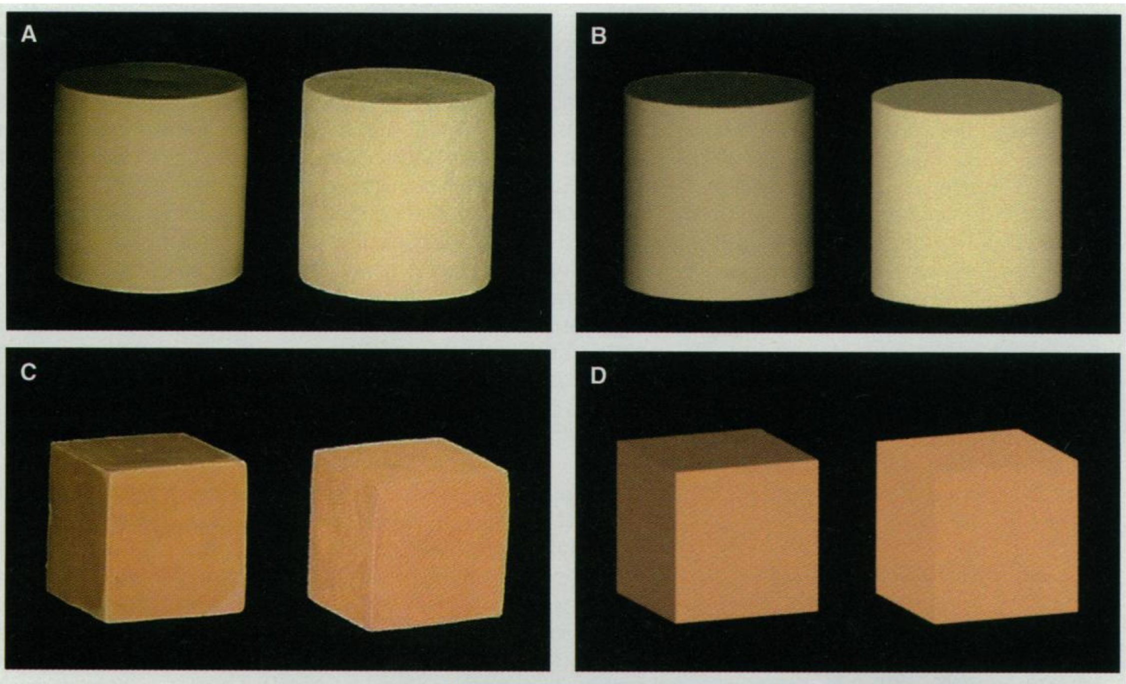

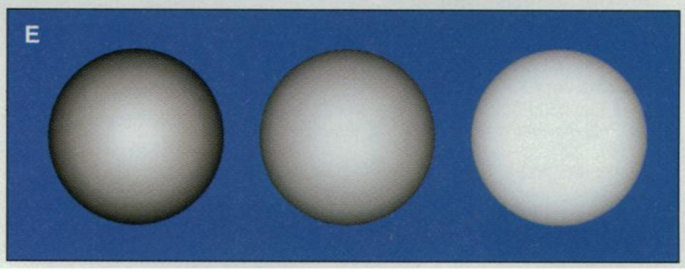

Fig. 4. (**A**) Video camera image of two cylinders made from exactly the same material (porcelain) and illuminated from approximately 10° above the camera. The right vase is much rougher than the left one, resulting in a flatter appearance. (**B**) Synthetic image of cylinders with similar dimensions, rendered with the theoretical model (left: $\sigma = 5°$, right: $\sigma = 35°$). (**C**) Camera image of two cubes made from stoneware, illuminated from approximately 18° to the left of the camera. (**D**) Synthetic image of cubes (left: $\sigma = 7°$, right: $\sigma = 40°$). In both camera and synthetic images, low macroscopic roughness of the left cube results in nearly Lambertian appearance, whereas very high roughness of the right cube results in all three faces producing almost the same brightness with clear edges no longer visible. The model and experiments suggest that for very high macroscopic roughness, when source and sensor directions are close to one another, all surface normals generate the same image brightness. Alternately, any object irrespective of its 3D shape produces just a silhouette, making it impossible to perceive shape. (**E**) Spheres illuminated and viewed from the same direction. As roughness increases (left to right: $\sigma = 0°$, $\sigma = 15°$, and $\sigma = 40°$) shading becomes flatter. For extreme roughness (far right), the sphere appears like a flat disc, as is observed in the case of a full moon.

$$L(\theta_r,\theta_i,\phi_r-\phi_i;\rho,\sigma) = \frac{\rho}{\pi}E_0 \cos\theta_i$$
$$\times \{A + B\mathrm{Max}[0,\cos(\phi_r-\phi_i)]\, \sin\alpha \tan\beta\} \quad (1)$$
$$A = 1.0 - 0.5\frac{\sigma^2}{\sigma^2 + 0.33}$$
$$B = 0.45\frac{\sigma^2}{\sigma^2 + 0.09}$$

where E_0 is the intensity of the source, (θ_r, ϕ_r) and (θ_i, ϕ_i) are the observer and illuminant directions in a coordinate frame with its z axis aligned with the surface normal, and $\alpha = \mathrm{Max}(\theta_r, \theta_i)$ and $\beta = \mathrm{Min}(\theta_r, \theta_i)$.

Our model may be viewed as a generalization of Lambert's law, which is simply an extreme case with $\sigma = 0$. The model has direct implications for shape recovery in machine vision (*28*) and for realistic rendering in computer graphics (*29*). Further, it provides a firm basis for the study of visual perception of three-dimensional (3D) objects. To illustrate this, we compared digital images of several objects constructed from materials such as porcelain and stoneware with synthetic images of the objects rendered by using the model (Fig. 4). The images closely matched. Both real and rendered shadings vary synchronously, and significantly, with macroscopic roughness.

These experiments have led to a curious observation: Our model predicts that for very high macroscopic roughness, when the observer and the illuminant are close to one another, all surface normals will generate approximately the same brightness. This implies that a 3D object, irrespective of its shape, will produce nothing more than a silhouette with constant intensity within. In the case of polyhedra, edges between adjacent faces will no longer be discernible (Fig. 4A), and smoothly curved objects will be devoid of shading (Fig. 1A). This visual ambiguity may be viewed as a perceptual singularity in which interpretation of the 3D shape of an object from its image is impossible for both humans and machines. This phenomenon offers a plausible explanation for the flat-disc appearance of the full moon (Fig. 4E).

REFERENCES AND NOTES

1. L. da Vinci, *Treatise on Painting*, A. P. McMahon, Trnsl. (Princeton Univ. Press, Princeton, 1959).
2. H. W. Janson, *History of Art* (Prentice-Hall and Abrams, New York, 1991).
3. D. S. Strong, *Leonardo on the Eye* (Garland, New York, 1979).
4. B. Geist, *Brancusi: The Sculpture and Drawings* (Abrams, New York, 1975).
5. J. H. Lambert *Photometria Sive de Mensura et Gradibus Luminus, Colorum et Umbrae* (Eberhard Klett, 1760).
6. P. Kubelka and F. Munk, *Z. Tech. Physik* **12**, 593 (1931).
7. S. Chandrasekhar, *Radiative Transfer* (Dover, New York, 1960).
8. V. S. Ramachandran, *Nature* **331**, 163 (1988).
9. B. K. P. Horn and M. J. Brooks, Eds., *Shape from Shading* (MIT Press, Cambridge, MA, 1989).
10. J. A. Smith, T. L. Lin, K. J. Ranson, *Photogramm. Eng. Remote Sensing* **46**, 1183 (1980).
11. M. F. Cohen and J. R. Wallace, *Radiosity and Realistic Image Synthesis* (Academic Press, Boston, 1993).
12. R. J. Woodham, *Opt. Eng.* **19**, 1 (1980).
13. J. J. Koenderink and A. J. van Doorn, *J. Opt. Soc. Am.* **73**, 6 (1983).
14. D. Forsyth and A. Zisserman, in *Proceeding of the IEEE Conference* on Computer Vision and Pattern Recognition, San Diego, CA, 4–8 June 1989 (IEEE, Los Alamitos, CA, 1989).
15. S. K. Nayar, K. Ikeuchi, T. Kanade, *Int. J. Comput. Vision* **6**, 3 (1991).
16. G. Westheimer, in *Medical Physiology*, V. B. Mountcastle, Ed. (Mosby, St. Louis, ed. 14, 1980), vol. 1, chap. 16.
17. E. Opik, *Publ. de l'Obs. Astron. de l'Univ. de Tartu* **26**, 1 (1924).
18. M. Minnaert, *Astrophys. J.* **93**, 403 (1941).
19. B. G. Smith, *J. Geophys. Res.* **72**, 16 (1967).
20. D. Buhl, W. J. Welch, D. G. Rea, *ibid.* **73**, 16 (1968).
21. R. G. Hering and T. F. Smith, *AIAA Prog. Astronaut. Aeronaut.* **23**, 337 (1970).
22. N. S. Orlova, *Astron. Zh.* **33**, 93 (1956).
23. R. Siegel and J. R. Howell, *Thermal Radiation Heat Transfer* (Hemisphere, Washington, DC, ed. 2, 1956).
24. B. W. Hapke and H. van Horn, *J. Geophys. Res.* **68**, 15 (1963).
25. Roughness, as defined here, is a purely macroscopic property. It is not indicative of the microscopic structure of the surface which is assumed to cause the surface to be locally Lambertian.
26. K. E. Torrance and E. Sparrow, *J. Opt. Soc. Am.* **57**, 1105 (1967).
27. Natural surfaces clearly profess a wide spectrum of macroscopic surface geometries. For deriving reflectance, a specific surface model must be assumed. In the past, several surface models (*19, 20*) have been found to be difficult to manipulate during reflectance model derivation. In the context of body reflection, radiance in the direction of the observer must be evaluated as an integral over all visible points on the surface patch projecting onto a single detector of the sensor. Because integration has the effect of weighted averaging, it turns out that several surface models are capable of capturing the primary reflectance characteristics of the surface. The V-cavity model (*21*) was chosen as it facilitates the analysis of pertinent radiometric and geometric phenomena and hence results in a reflectance model that performs fairly well for a large variety of real surfaces.
28. M. Oren and S. K. Nayar, *Int. J. Comput. Vision*, in press.
29. ———, in *Proc. ACM SIGGRAPH* (1994).
30. B. W. Hapke, R. M. Nelson, W. D. Smythe, *Science* **260**, 509 (1993).

31. This work was supported by an ARPA grant and a David and Lucile Packard Fellowship to S.K.N. and an IBM Graduate Fellowship to M.O. We thank V. Nalwa of Bell Laboratories and A. Aggarwal, M. Lai, and S. Baker of Columbia University for valuable suggestions. Thanks to S. Nene of Columbia University for assistance with the images.

9 September 1994; accepted 1 December 1994

Requirement of Carbon Dioxide for in Vitro Assembly of the Urease Nickel Metallocenter

Il-Seon Park and Robert P. Hausinger*

Assembly of protein metallocenters is not well understood. Urease offers a tractable system for examination of this process. Formation of the urease metallocenter in vivo is known to require four accessory proteins: UreD, postulated to be a urease-specific molecular chaperone; UreE, a nickel(II)-binding protein; and UreF and UreG, of unknown function. Activation of purified *Klebsiella aerogenes* urease apoprotein was accomplished in vitro by providing carbon dioxide (half-maximal activation at ~0.2 percent carbon dioxide) in addition to nickel ion. Activation coincided with carbon dioxide incorporation into urease in a pH-dependent reaction ($pK_a \geq 9$, where K_a is the acid constant). The concentration of carbon dioxide also affected the amount of activation of UreD-urease apoprotein complexes. These results suggest that carbon dioxide binding to urease apoprotein generates a ligand that facilitates productive nickel binding.

Urease, the first enzyme crystallized (*1*) and the first shown to include nickel (*2*), is found in certain plants, fungi, and bacteria. It participates in environmental nitrogen transformations and is a virulence factor in certain pathogenic microbes (*3*). According to x-ray absorption spectroscopic analysis (*4*), the protein contains a dinuclear Ni(II) active site (*5*) in which each metal atom has a Ni(imidazole)$_x$(N,O)$_{5-x}$ (x = 2 or 3) coordination environment. In vivo assembly of this metallocenter in *K. aerogenes* (*6*) involves the participation of four accessory gene products: UreD, UreE, UreF, and UreG (*7*).

UreD has been postulated to function as a molecular chaperone that stabilizes a urease apoprotein conformation that is competent for nickel incorporation (*8*). Evidence consistent with this hypothesis includes (i) our ability to purify several forms of a UreD-urease apoprotein complex of the formula (urease)$_3$UreD$_n$, where (urease)$_3$ is the native $(\alpha\beta\gamma)_3$ protein (n = 1, 2, or 3); (ii) the demonstration that these complexes can be partially activated by addition of nickel ions (increasing amounts of activation correlate to increasing n); and (iii) the finding that UreD dissociates from urease during activation. UreE has been proposed to serve as a

Departments of Microbiology and Biochemistry, Michigan State University, East Lansing, MI 48824, USA.

*To whom correspondence should be addressed.